Batteries & Supercaps
Research Article
doi.org/10.1002/batt.202400743
Chemistry Europe
European Chemical Societies Publishing
www.batteries-supercaps.org

Recessed Microelectrodes as a Platform to Investigate the Intrinsic Redox Process of Prussian Blue Analogs for Energy Storage Application

Nomnotho Jiyane+,[a] Carla Santana Santos+,[a] Igor Echevarria Poza,[b] Mario Palacios Corella,[b] Muhammad Adib Abdillah Mahbub,[a] Gimena Marin-Tajadura,[c] Thomas Quast,[a] Maria Ibáñez,[b] Edgar Ventosa,[c] and Wolfgang Schuhmann*[a]

The determination of the intrinsic properties of solid active material candidates is essential for their performance optimization. However, macroscopic electrodes and related analytical techniques show challenges concerning the number of additional influencing parameters. We explore recessed microelectrodes (rME) as a platform that allows for a binder-free investigation of Prussian Blue analogues (PBA), a family of promising battery materials. The enhanced diffusion using microelectrochemical tools is indispensable to assess the intrinsic material performance, overcoming the limitation of cation diffusion from the electrolyte to the solid interface during (dis)charging cycles and allowing the investigation of limiting steps in the coupled ion-electron transfer process. The intrinsic electrochemical performance of PBAs was studied in a three-electrode configuration by means of cyclic voltammetry and galvanostatic (dis)charging in aqueous Na^+-containing electrolyte. We extended the evaluation to the role of the electrolyte on the performance of cathodic and anodic processes of a Mn-based PBA. Ex-situ and operando chemical characterization were coupled to support the microelectrochemical results.

Introduction

The use of electrochemical energy storage devices based on scarce elements, i.e.: Li^+, has pushed the battery development to the exploration of new active materials, such as Na^+- and K^+-based chemistries. Active materials capable of storing Na^+ or K^+ within their structures have been recommended for Na-ion batteries (SIB) and K-ion batteries (KIB). Among the active materials for the cathode, Prussian Blue analogs (PBAs) exhibit affordable and scalable synthesis routes and stability in aqueous electrolytes.[1] PBAs possess a porous three-dimensional structure, an open framework with zeolitic characteristics, which allows the insertion of alkali metal ions[2] with minimal structural changes, thus leading to a reversible intercalation/deintercalation process,[3,4] and hence PBAs have been explored as solid active materials for SIBs,[5,6,7] or supercapacitors.[8,9,10] The elemental composition of the PBAs defines the redox potential of the PBA processes which can therefore be adjusted to obtain positive or negative electrode materials. For instance, Mn- and Cr-based PBAs show comparatively lower potential values,[11,12,13] and the properties of these materials became attractive for sensor applications,[14] for electro-driven ion separation,[15] and redox-mediated flow batteries.[16] PBAs were mainly suggested as cathode materials, and the design of PBA as anode materials with high stability is still a challenge.[13] Despite the wide applicability of PBAs, they are prone to degradation, e.g. due to dissolution processes in dependence on cation and anion composition and the redox process.[17,18] Therefore, designing and characterizing new PBAs and varying the electrolyte composition is required. Conventional macroelectrode-based electrochemical methods were used to investigate the electrochemical performance of active materials for energy storage.[7] However, mass transport limitation and other experimental factors such, as using binders and conductive inks influence the electrochemical properties, making it complex to evaluate the intrinsic active material performance. Micro- and nanoelectrochemical tools were suggested to prevent these complex additional matrix effects by confining the active material and eliminating the influence of ink formulations during electrocatalysis[19,20,21,22] or sensor studies.[23] By confining the electroactive material at the surface of a micro- or nanoelectrode, enhanced mass transport is assured,[24,25,26] replacing forced convection techniques such as rotating disk electrode

[a] N. Jiyane,+ C. Santana Santos,+ M. A. Abdillah Mahbub, T. Quast, W. Schuhmann
Analytical Chemistry – Center for Electrochemical Sciences (CES), Faculty of Chemistry and Biochemistry, Ruhr University Bochum
Universitätsstraße. 150, D-44780, Bochum (Germany)
E-mail: wolfgang.schuhmann@rub.de

[b] I. Echevarria Poza, M. Palacios Corella, M. Ibáñez
Institute of Science and Technology Austria (ISTA), Am Campus 1, 3400 Klosterneuburg, Austria

[c] G. Marin-Tajadura, E. Ventosa
Department of Chemistry, University of Burgo, Pza. Misael Bañuelos s/n, 09001 Burgos (Spain)

[+] These authors equally contributed to this work

Supporting information for this article is available on the WWW under https://doi.org/10.1002/batt.202400743

(RDE) experiments. Moreover, confining the active material in a recessed microelectrode offers several practical advantages, such as the consumption of a very small amount of the material and rapid preparation.[27,28] The investigation of the intrinsic performance of a solid material with micro- or nanoelectrochemistry can contribute to understand the complexity of coupled ion-electron transfer reactions.[29] Recently, we have confined Prussian blue (PB) inside the cavity of a recessed carbon nanoelectrode to ensure fast kinetics of the redox process of the solid material, allowing the interrogation of the reaction between the solid material, PB, and a dissolved redox species, an essential reaction in the context of mediated redox flow batteries.[30] Such strategies rely on the electrodeposition of the active material from precursor electrolytes[30,31] to investigate the intrinsic redox processes of a specific solid active material.

Investigating a wider range of materials, such as as-synthesized powders, with respect to their performance as energy storage materials requires new micro-electrochemical tools.[22,32] We propose the use of recessed microelectrodes (rMEs) as a tool for accelerated investigation of the intrinsic redox processes of as-prepared PBA powders including the performance evaluation in different electrolyte compositions for aqueous Na-based energy storage technologies. The synthesized active materials can be directly confined into the rME as previously demonstrated in other studies,[33] in electrocatalysis,[19,22] and sensors,[23] but it has not been reported for the evaluation of the electrochemical performance of PBAs for energy storage applications. The capability of this strategy is first demonstrated by using a known cathode PBA material for aqueous Na-ion batteries, namely nickel hexacyanoferrate (NiHCF). The intrinsic material performance during 100 cycles and a C-rate of 26 C exhibits a coulombic efficiency (%CE) of 98% and a discharge capacity retention of 90%. The proposed strategy is then extended to evaluate the intrinsic performance of a Mn-based PBA for the cathode and anode in different Na^+-containing electrolytes supported by ex-*situ* and *operando* chemical characterization to comprehend dissolution and structural changes of the Mn-based PBA.

Results and Discussion

The fabrication of recessed microelectrodes (rMEs) involves first the electrochemical etching of a gold disc microelectrode (diameter 100 μm).[24] More experimental details can be found in the supporting information (SI). The PBA powder was loaded into the cavity of the rME by mechanically compressing the material. The amount of the loaded solid active material can be flexibly controlled by the depth of the recession of the microelectrode, which can be tuned by the etching time, and was about 16 μm derived by scanning electron microscopy (SEM) and the voltammetric response of a free-diffusing redox probe (Figure S1.1). To ensure a similar mass loading throughout the measurements, the same rME was used in the PBA tests. The rME was cleaned by sonication in ethanol after each measurement.

Scheme 1a depicts the fabrication of the rME and the subsequent filling with the solid material. The rME filled with PBA (PBA@rME) was used as the working electrode in a three-electrode set-up (Scheme 1b and Figure S1.2) for evaluating the performance of the PBA during (dis)charging cycles. The ability to investigate the material properties using the rMEs was first demonstrated using NiHCF, a PBA used as cathode material in Na^+-based batteries. The small changes upon cycling and the preserved framework of NiHCF are of great importance for its use in a long-life rechargeable Na^+ battery. The reported nominal capacity of NiHCF is around 60 mAh/g,[5] with some recent strategies to enhance its capacity.[34] In NiHCF, Ni^{II} is electrochemically inactive, but it provides matchless stability in the PBA lattice.[35] Moreover, NiHCF features larger channels compared to the size of the Na^+-ion, allowing its easier insertion,[35] thereby facilitating mass transport and improving stability upon cycling. Figure S2.1 shows an SEM image of NiHCF assorted shapes and non-uniform sizes as well as the X-Ray diffraction (XRD) pattern, which is in agreement with those reported previously, specifically the number of intense peaks observed at NiHCF.[36] These peaks were determined as an octahedral coordinated framework. During the redox process of PBA, the (de)insertion of alkali metals occurs in the PBA structure. Therefore, the cation role is directly related to the

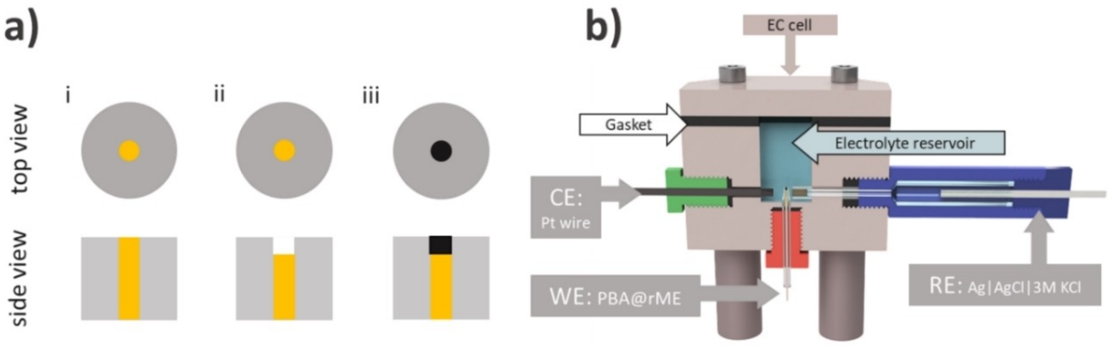

Scheme 1. a) Gold disc microelectrode i) before, ii) after the etching process, and iii) recessed microelectrode filled with the active solid material (PBA). b) A scheme of the closed electrochemical cell (EC) used to test the solid material within the rME (PBA@rME). The working electrode (WE), the reference electrode (RE), and the counter electrode (CE) were positioned in the closed cell by screws and gaskets.

Research Article
doi.org/10.1002/batt.202400743
Chemistry Europe
European Chemical Societies Publishing

PBA capacity and stability upon cycling. Controversially, the anion has also been considered a factor in PBA stability by potentially adsorbing at the structural edges during charging and contributing to the degradation processes of PBA.[31] Initially, the electrochemical behavior of as-prepared NiHCF was registered by cyclic voltammograms (CVs) in a highly concentrated $NaClO_4$ solution, demonstrating it as a promising electrolyte to NiHCF redox processes.[31] Control experiments performed with the empty rME (in the absence of any PBA) did not show any reversible redox process in voltammograms in the different Na^+-containing electrolytes (Figure S1.3).

The redox process of NiHCF@rME in 5 M $NaClO_4$ electrolyte was stable during 2000 cycles with a potential peak separation of ~76 mV and an oxidation/reduction peak current ratio of 0.9 (Figure 1a). Moreover, the material confined within the rME ensures diffusion of the Na^+ ions to the solid material, allowing high scan rates in cyclic voltammetry. To highlight the effectiveness of this methodology, a galvanostatic evaluation of NiHCF@rME was subsequently carried out in 5 M $NaClO_4$. Galvanostatic cycles performed using conventional macroelectrode-based electrochemical methods are typically carried out at a slow C-rate, i.e. in the range of 0.3 C–0.8 C,[1,37] which is insufficient to distinguish different processes with different kinetics. The coupled ion-electron transfer reaction at a solid material in energy storage devices has a high complexity, and the limiting steps can be a convolution of i) ion diffusion from the bulk electrolyte to the solid particles, ii) ion diffusion within solid particles, iii) the electron transport from the current collector to the solid surface interface, iv) the electron transport within the solid, and v) the coupled ion-electron transfer reaction. Using microelectrochemistry, Na^+ diffusion from the bulk to the solid surface is enhanced and presumably not any longer limiting which allows gaining understanding of the electron/ion transfer reactions occurring in the material. Charging-discharging cycles were performed in a wide C-rate range: from 3 C to 70 C, for 5 cycles. Figure S2.2 shows the galvanostatic charging profiles of NiHCF@rME at different C-rates. In order to deconvolute the effect of electrical conductivity between the solid particles, rME were prepared by grinding the 80%wt NiHCF mixed with 20%wt of carbon black (C65, TIMCAL) as a conductive additive, named NiHCF + C_{65}@rME. While the intrinsic capacity retention (CR) ratio of the material dropped in the absence of carbon to 70% at around 10 C and to 55% at 20 C, the capacity ratio was remarkably kept above 90% at 20 C for the NiHCF + C_{65}@rME (Figure 1b). This indicates that the electrical conductivity between the solid particles plays a critical role as long as sufficient ion transport in the electrolyte is ensured. At 70 C, the capacity retention of NiHCF + C_{65}@rME reached around 60%. The drastic capacity change at a high C-rate is due to the charge transfer process at the solid particle. At a low C-rate, the charge transfer process combines the sum of ion mobility and electron mobility as well as the conversion of the redox centers inside the particle.[29] Note that the recessed area of the microelectrode is in the range of some μm, ensuring fast ion transport in the electrolyte to the confined material, but does not exclude the contribution of the material porosity and tortuosity, which could be a limitation at high C-rate. The nominal capacity of NiHCF was used to estimate the amount of active material inside the rME. Using the capacity value of 3.25 nAh at 3 C, the active mass was calculated to be

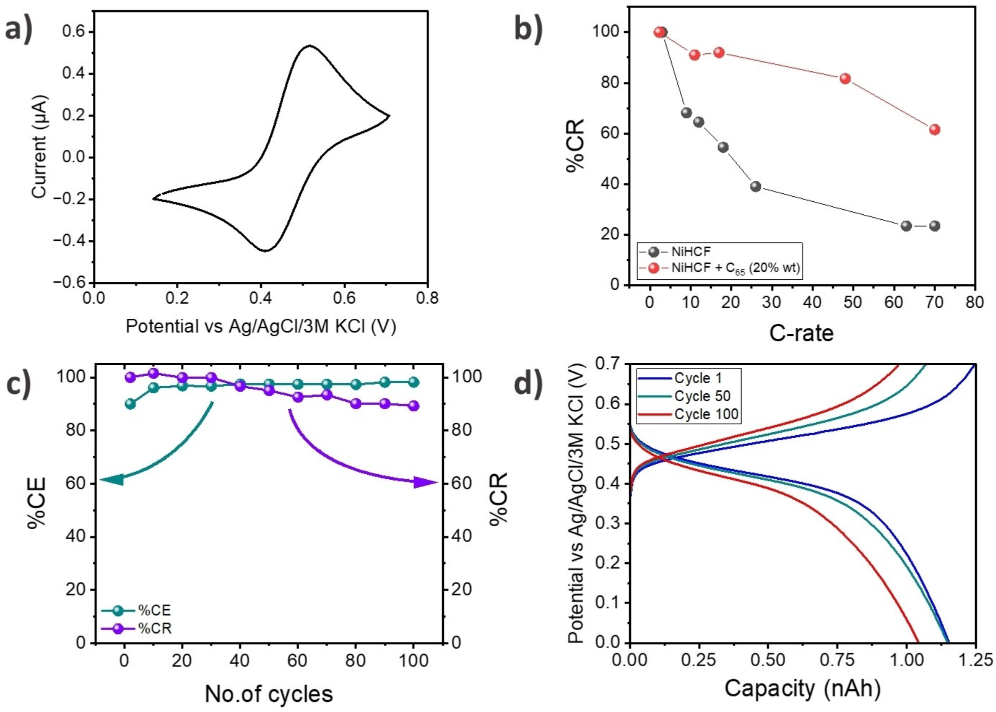

Figure 1. NiHCF performance using the NiHCF@rME. Electrochemical tests were performed in 5 M $NaClO_4$, a) Cyclic voltammogram with a scan rate of 100 mV/s, galvanostatic charging and discharging cycles resulted in b) Capacity retention (%CR) at different C-rates black NiHCF and red NiHCF mixed with 20% C65. c) Coulombic efficiency (%CE and %CR) test performed at 26 C), d) capacity at different cycles for the NiHCF@rME (no addition of C65).

Research Article
doi.org/10.1002/batt.202400743
Chemistry Europe
European Chemical Societies Publishing

around 55 ng. Galvanostatic cycling at a charging rate of 26 C was employed to evaluate the intrinsic stability of NiHCF during cycling. This allows insight into the robustness of the micro-electrochemical platform during accelerated testing. Even under these conditions, the NiHCF@rME were able to charge at a high C-rate (26 C) while maintaining high coulombic efficiency (CE: 98%) throughout 100 cycles (Figure 1c). After 100 cycles, the capacity retention was around 90% of the capacity recorded in the first cycle (Figure 1c, d).

The proposed analytical strategy of using the rME and its advantages were demonstrated by performing an accelerated cycling test with a small amount of the material reaching a high CE at a high C-rate for up to 100 cycles. Therefore, we were convinced that the methodology could be transferred to investigate other PBAs. We investigated the stability of two Mn-based PBA in Na^{+}-containing electrolytes, namely Mn^{III} hexacyanoferrate (MnHCF), and Mn^{II} hexacyanomanganate (MnHCMn). MnHCF has been previously suggested as cathode material for SIB (high voltage cell) because of its high specific capacity, processing capability, and cell operation.[18] However, the long-term stability of this material appears to be rather poor. A possible explanation could be the partial oxidation of MnHCF resulting in the formation of Mn^{III}, which is likely to undergo disproportionation in the presence of the aqueous electrolyte to form MnO and Mn^{II},[38] which is a well-known complexity in Mn-based systems.[2,38,39] The physical characterization of MnHCF was performed by means of SEM and XRD (Figure S3.1), showing the cubic structure and its polydispersity with sizes varying from 100 nm to 600 nm. As-prepared MnHCF was confined within the rME and the intrinsic material performance was tested in different Na-based electrolytes and at varying concentrations. Firstly, the performance of the material was evaluated by recording consecutive cyclic voltammograms at a scan rate of 100 mV/s in a potential range restricted to the oxidation of the Fe center. The rME was newly filled with the PBA for each electrochemical test. Figure 2a–b shows the CVs recorded in 1 M NaCl and 1 M $NaClO_4$ as electrolytes. Interestingly, the performance of MnHCF@rME in low-concentration electrolytes presented a much faster loss of activity within only 90 CV cycles. The redox potential shifted by around 5–10 mV to more anodic potentials in both electrolytes upon cycling. The peak shift suggests changes occurring at the structural framework of the MnHCF even in the controlled potential range, which can be linked to the decrease of intrinsic activity observed during the initial cycles. Interestingly, the variation of the redox potential of MnHCF upon cycling was slightly dependent on the electrolyte concentration. The potentiostatic evaluation also revealed an improved stability of the MnHCF activity during cycling in highly concentrated (5 M) electrolytes (Figure 2c–d). The evaluation was extended to up to 3000 cycles in 5 M $NaClO_4$ (Figure S3.2). The MnHCF performance decays after 3 h (around 675 cycles), as derived from the charge of the oxidation peak (Figure S3.3). This chemical instability poses a challenge in a practical battery cell as it affects the long-term cycling of this material. Galvanostatic cycling at 20 C was carried out in 5 M $NaClO_4$ in a similar potential range. The coulombic efficiency and discharge capacity retention declined by around 30% during 40 consecutive cycles (Figure 2e). The performance of MnHCF differs from that of the NiHCF, presenting a loss of intrinsic capacity just after a few cycles. The loss of capacity was further observed in the discharge capacity plot, with a constant loss observed from the 1^{st} to the 40^{th} cycle, reaching a total loss of 28% (Figure 2f).

The redox potential capacity profile initially showed a distinct potential plateau during the first cycles, which evolved into two separate plateaus after 30 cycles. This change is likely related to a redox process of the Mn-redox center modulating the integrity of the MnHCF. Similarly, the optical evaluation of the rME indicated a change in the amount of the material inside the recessed area after the electrochemical measurements (see Figure S3.4). Note that **no** conclusion can be made whether the material suffered loss of electrical contact or dissolution. Nevertheless, at this point, it remained unclear whether the decrease in capacity was due to a loss of intrinsic activity or a loss of the active material. Therefore, several factors were taken into account to monitor the potential dissolution. The electrolyte was analysed for trace elements using inductively coupled plasma mass spectrometry (ICP-MS) before and after the electrochemical measurement. The relative concentration of Mn and Fe of the initial electrolyte and after cycling revealed a dissolution of the MnHCF during cycling, as summarised in Table 1.

Moreover, *operando* Raman spectroscopy was employed to monitor structural changes during cycling. Raman spectra were recorded for the MnHCF material deposited on a glassy carbon plate over a broad wavelength range as a control measurement. The Raman spectra (Figure S3.5) show a band at 500–600 cm^{-1} that correlates to Mn metal, and as expected, the characteristic peaks of Fe^{2+}–CN–Mn^{2+} and Fe^{2+}–CN–Mn^{3+} were observed at 2169 cm^{-1}.[6,40] MnHCF was then confined inside the rME and positioned in an upside-down electrochemical cell adapted for *operando* Raman microspectroscopy,[33] see scheme in Figure 3a. The bands visualized in the control spectra were consistent with the ones recorded when the material was confined within the rME. Figure 3b shows the Raman spectra obtained after assembling the MnHCF@rME in the cell at open-circuit potential (OCP), after one CV cycle, and after several galvanostatic (dis)charge cycles at 72 C. In the presence of the electrolyte, the band at 1617 cm^{-1} can be ascribed to O–H and H–O–H bending and vibration modes.[6,41] During the *operando* electrochemical Raman microspectroscopy, the band associated with the PBA (2169 cm^{-1}) progressively vanished as the number of cycles increased, see Figure 3b. Simultaneously, a loss of coulombic efficiency was registered at cycle numbers >10 (Figure 3c) along with the vanishing of the Fe–CN–Mn band. This indicates

Table 1. Ex-situ ICP-MS values indicating the amount of dissolved Mn and Fe from MnHCF before and after galvanostatic cycling.

Concentration (ppb)	Initial electrolyte	Electrolyte after cycling
Mn	≈7.8	≈26.7
Fe	≈3.2*	≈11.3

* Value below the limit of detection.

Research Article
doi.org/10.1002/batt.202400743

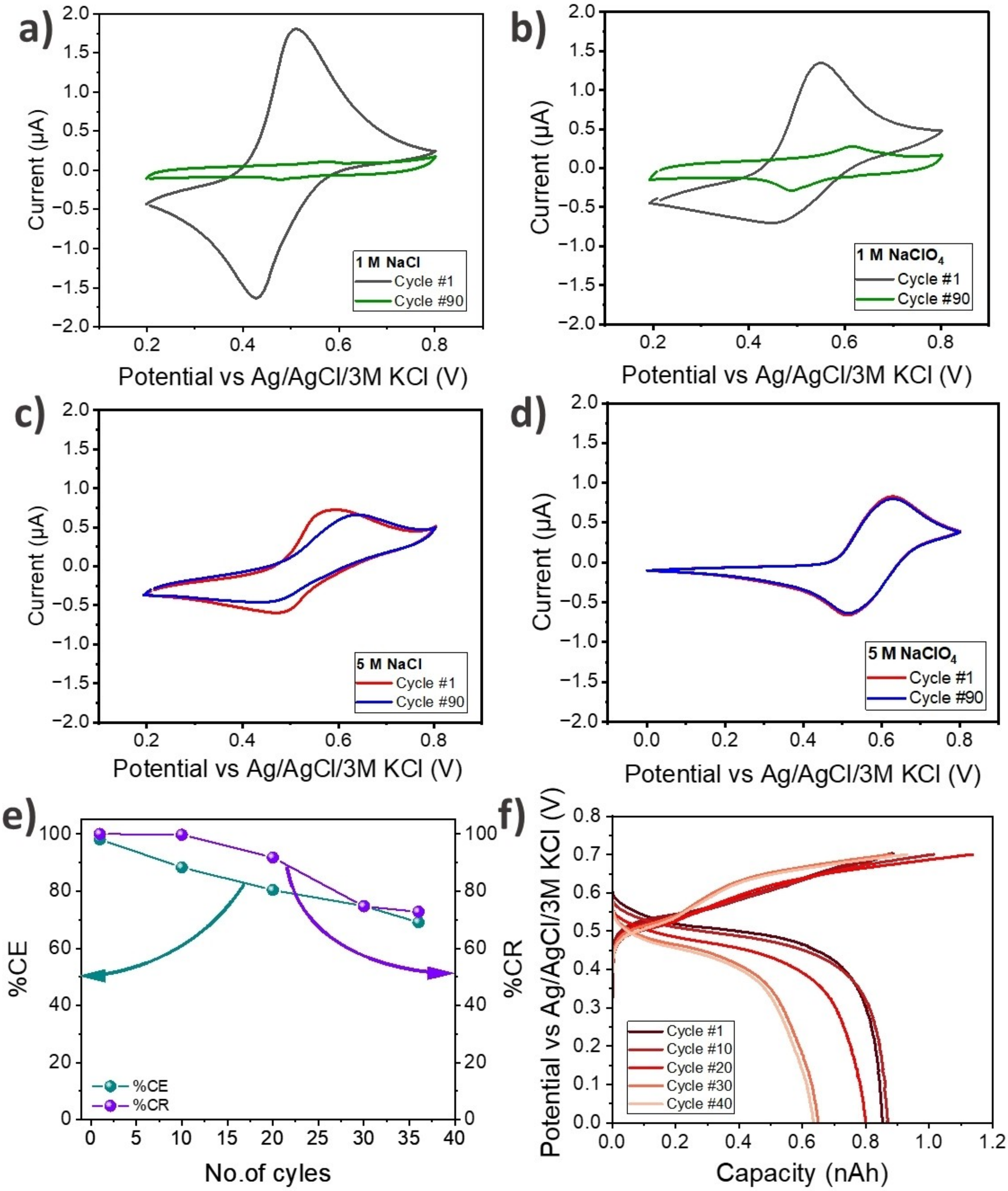

Figure 2. Electrochemical test of MnHCF@rME. CVs at 100 mV/s in a) 1 M NaCl, b) 1 M $NaClO_4$, c) 5 M NaCl, and d) 5 M $NaClO_4$. e) galvanostatic charging coulombic efficiency (%CE) and discharge capacity retention (%CR) at 20 C. f) Capacity plot of the (dis)charge cycles.

that materials degradation during cycling of MnHCF@rME, which we attribute to the dissolution process based on the visual analysis of the recessed electrode after cycling (Figure S3.4), supported by the ICP-MS and Raman spectroscopy. The presence of water in the MnHCF framework alters its structure and influences the material's electrochemical properties.[42] Moreover, the high content of lattice-bound water in the PBA structure results in a low number of vacancies available for Na^+ insertion and, hence, the CE and capacity decrease.[43]

Finding new PBA candidates may improve an electrochemical power device by tuning the potential of the electrochemical process. In this regard, PBAs were proposed with different metals (other than iron) assuming the C- and the N-coordinated transition metal in the PBA structure.[18] In this aspect, Mn (II) hexacyanomanganate (MnHCMn) was shown as a PBA reaching a high capacity (209 mAh/g) in a non-aqueous Na-ion system and being capable of undergoing a reduction and oxidation process combined with cation intercalation.[44] The material, however, reached a cycling stability of 78.3 % after

Research Article
doi.org/10.1002/batt.202400743

Chemistry Europe
European Chemical Societies Publishing

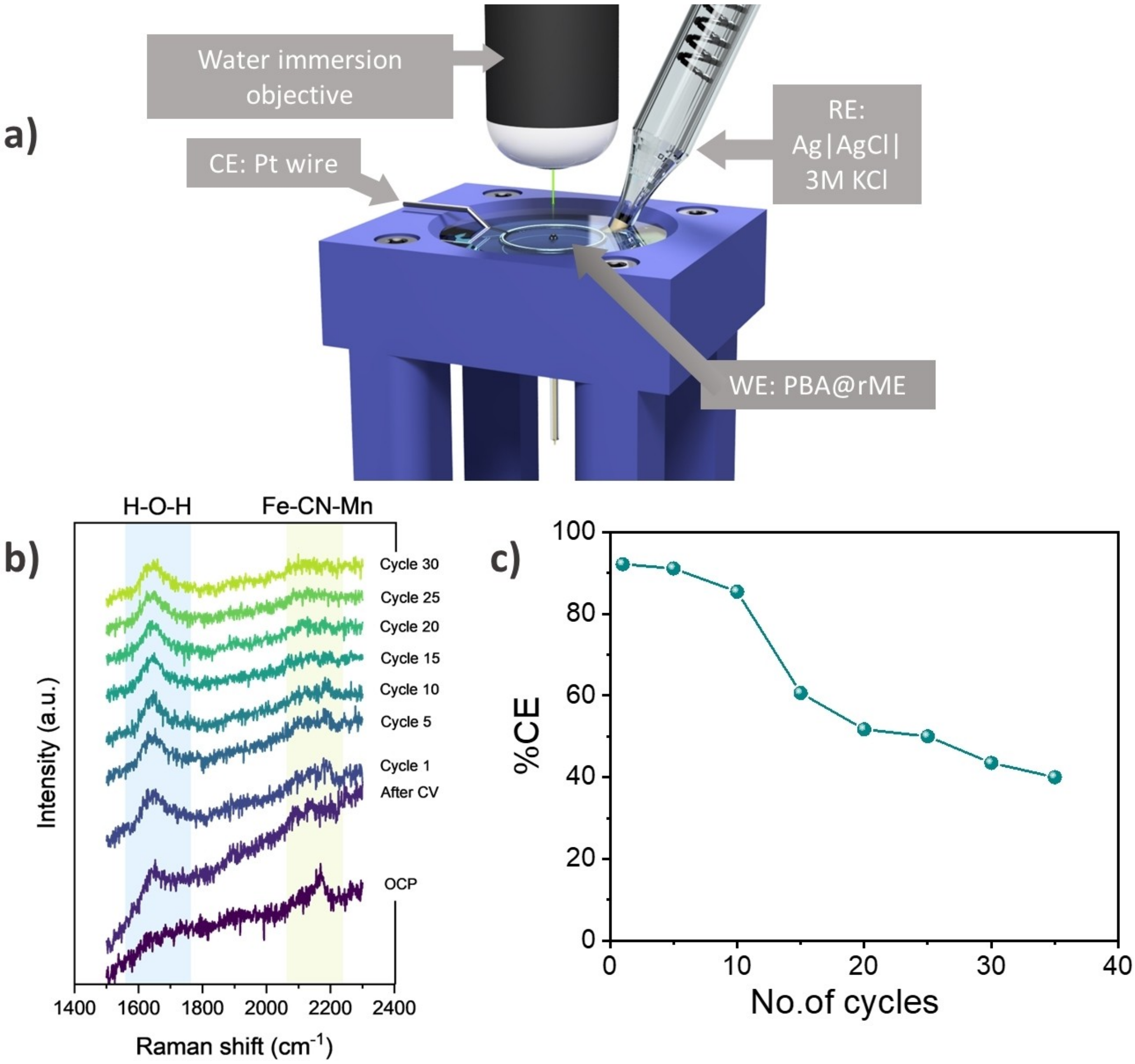

Figure 3. MnHCF@rME operando microelectrochemical Raman spectroscopy measurement. a) Illustration of the upside-down PBA@rME centered to the water immersion objective in the electrochemical cell (not drawn to the scale). b) Raman spectra during galvanostatic cycles at 72 C, and c) %CE.

100 cycles (0.2 C) in 1 M $NaClO_4$/propylene carbonate. In an aqueous electrolyte, the redox process (Mn II–NC–Mn II/I) competes with H_2 evolution, locally changing the pH and contributing to the degradation of the MnHCMn by the replacement of CN^- with OH^-. Pasta *et al.* demonstrated the use of MnHCMn in a full cell exploring the process (Mn II–NC–Mn III/II) at a lower overpotential in 10 M $NaClO_4$ and the presence of an additive, $Mn(ClO_4)_2$.[45] We have employed the rME capability of enhancing the diffusional mass transport towards the PBA surface to investigate the influence of the electrolyte regarding MnHCMn (Mn II–NC–Mn II/I) stability in aqueous electrolytes. Details of the MnHCMn synthesis and characterization can be found in the experimental section and SI (Figure S4.1). The intrinsic electrochemical behavior of the synthesized MnHCMn was obtained upon testing the active material in different aqueous Na^+-containing electrolytes. The specifically designed electrochemical cell for rME measurements was placed inside a glass chamber (see scheme in Figure S4.2), which was continuously purged with Ar to ensure an inert atmosphere. Solvation and solubility effects are the main parameters governing the potential of a PBA for electron-transfer coupled reactions together with alkali metal intercalation.[46] For this reason, the anion nature also affects the PBA performance. Cyclic voltammetry showed the ability of MnHCMn to reversibly host Na^+ in its framework in electrolytes with Cl^-, SCN^- and ClO_4^- as anions (Figure S4.3).

The performance of each electrolyte was examined by extended cycles up to 1500 at 100 mV/s. The charge decreased during sequential cyclic voltammograms, demonstrating that MnHCMn lost its activity upon cycling. Optical verification showed the presence of MnHCMn inside the rME (Figure S4.4). Furthermore, potentiostatic cycling indicated a peak potential separation of 110–120 mV in the Na^+-based electrolytes, confirming the quasi-reversible behaviour in all the electrolytes. MnHCMn@rME was employed to perform a galvanostatic charging test in a three-electrode configuration. The coulombic

Research Article
doi.org/10.1002/batt.202400743

efficiency varied from 10% to 14% and to 20% in 1 M NaCl, 1 M $NaClO_4$, and 1 M NaSCN, respectively (Figure S4.3). Therefore, the MnHCMn performance was further evaluated in different concentrations of NaSCN as electrolyte. Figure 4a shows the representative cyclic voltammograms registered in 1 M, 5 M, and 10 M NaSCN. While the change of the redox peak potential ($\approx$100 mV) to a more positive potential with increasing concentration was excepted based on the Nernst shift, a notable feature is the wider peak in the electrolyte with higher ionic strength. The ratios between cathodic and anodic peak current (i_p ratio) were determined as 0.74, 0.87, and 0.91 in 1 M, 5 M, and 10 M NaSCN, respectively, showing a trend to increased reversibility in highly concentrated electrolytes. Moreover, the potential separation between the peak currents was 135 mV, 115 mV, and 100 mV, respectively, in 1 M, 5 M, and 10 M NaSCN. Interestingly, the ionic strength of the electrolyte affected the redox peak current. In 1 M NaSCN, the MnHCMn redox processes showed an oxidation peak current of 1 µA, whereas for 5 M the current reached just 0.5 µA, and in 10 M NaSCN a decreased redox peak current of only 0.25 µA remained. This effect could be associated with the increased electrolyte viscosity at higher ionic strengths, as shown before to aqueous NaSCN electrolyte,[47] which likely decreased the ion mobility and affected the Na^+ diffusion. Recently, the same trend on the current was reported in a study of ferrocene as redox probes at different tetrabutylammonium hexafluorophosphate ($TBAPF_6$) concentrations in propylene carbonate.[48] Furthermore, voltammograms at different scan-rate were registered in different NaSCN concentrations (Figure S4.5 Interestingly, the followed great linearity as predicted by the Randles-Sevcik equation i_p increased linearly with the scan rate for 1 M and 5 M NaSCN ($R^2 > 0.99$). The Na^+ diffusion coefficients into the PBA structure were estimated to be 1.3×10^{-17} $cm^2 s^{-1}$ for 1 M and 2.6×10^{-19} $cm^2 s^{-1}$ for 5 M NaSCN, respectively, supporting that highly concentrated electrolytes reduce ion diffusion within the material. Note that the experiments were carried out with the PBA in the absence of any conductive material. The evaluation in 10 M NaSCN resulted in a deviation of linearity in the Randles-Sevcik plot, suggesting adsorption processes.

The MnHCMn redox processes were monitored at different NaSCN electrolyte concentrations to evaluate the contribution of the Na^+ ionic strength and water availability. The stability of MnHCMn in NaSCN electrolytes was investigated by galvanostatic cycling with the rME. Figure 4b summarises the galvanostatic %CE in different NaSCN concentrations at 20 C. More

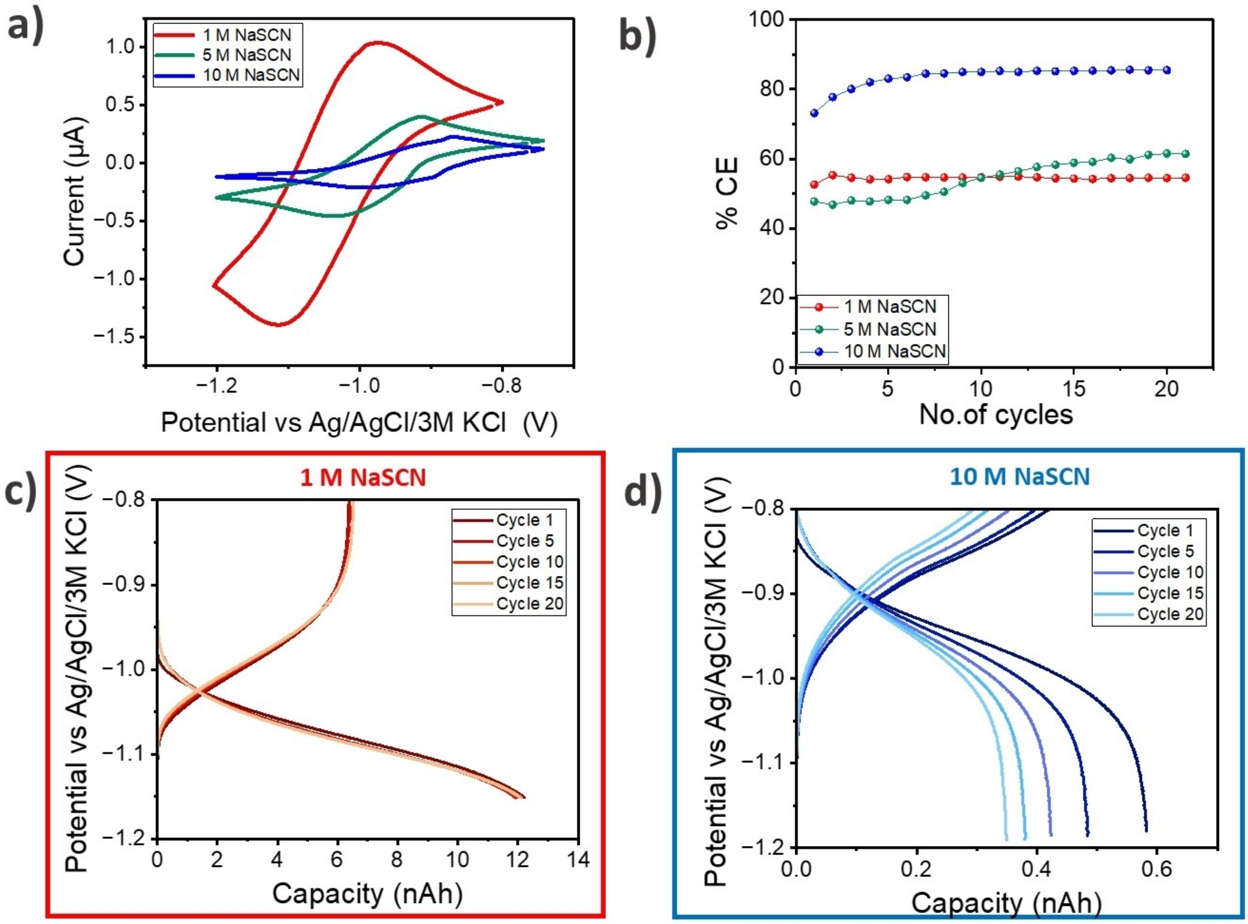

Figure 4. Electrochemical performance of MnHCMn. a) Cyclic voltammograms recorded with a scan rate of 100 mV/s in different NaSCN electrolyte concentrations. b) %CE at various NaSCN electrolyte concentrations. c) Capacity vs potential plot in 1 M NaSCN, and d) in 10 M NaSCN. Galvanostatic tests were run at 20 C.

Research Article
doi.org/10.1002/batt.202400743
Chemistry Europe
European Chemical Societies Publishing

details of the galvanostatic cycling using the MnHCMn@rME can be found in Figure S4.6.

Interestingly, the average %CE remained unchanged throughout the cycling at 54%–63% for 1 M NaSCN and slightly increased to 60%–75% in 5 M NaSCN. A clear change occurred when the galvanostatic cycling of MnHCMn was performed in 10 M NaSCN, where the %CE reached a high value of 80%–90%. These results demonstrate that increasing the concentration of NaSCN improves the coulombic efficiency, probably due to the higher availability of Na^+ and lower amount of free H_2O due to undercoordination. On the other hand, the capacity followed the reverse behavior. In 1 M NaSCN, MnHCMn@rME retained the highest capacity followed by 5 M and then 10 M, with the capacity in the 1 M electrolyte being 30 times higher than the one registered in 10 M NaSCN (Figure S4.7). The capacity remained constant in 1 M NaSCN after 20 cycles, despite the low CE (Figure 4c). The opposite was observed during cycling MnHCMn@rME in 10 M NaSCN, where the capacity dropped to almost half its initial value within just 20 cycles. Considering the amount of material within the rME (about 55 ng), the capacity of MnHCMn in 1 M NaSCN reached values of 190 mAh/g (20 C), which is in a similar range as that obtained at 0.2 C reported before.[44] The estimated capacity of MnHCMn dropped from 12 to 7 mAh/g during cycling in 10 M NaSCN. Geng *et al.* observed a similar correlation between the electrolyte concentration and the capacity for a $NaNiCoMnO_2$ (NaNCM) cathode in 0.1, 1, and 3 M NaTFSI electrolytes.[49]

This indicates that at high electrolyte concentrations, other factors have to be considered, such as low ion mobility, ion migration, and ion conduction.[50] Moreover, the influence of side reactions with O_2 was further investigated by evaluating the performance of MnHCMn@rME in a 10 M NaSCN in the presence and absence of O_2 (Figure S4.8). The %CE dropped from 95% (no O_2) to 70% (with O_2) which suggests side reactions of MnHCMn, and the importance of performing the experiments in the absence of O_2.

Conclusions

The recessed microelectrode (rME) platform offers a novel approach to studying the electrochemical performance of solid active materials for energy storage. The intrinsic electrochemical properties of PBA hosted in the rME were investigated by combining potentiostatic and galvanostatic methods with the main focus on Na^+-intercalation technologies. To demonstrate the capability for accelerated material evaluation using the rME platform, NiHCF exhibited optimal conditions in 5 M $NaClO_4$, with high CE values (above 90%) during galvanostatic (dis)charging cycles and it retained 90% of its capacity at a fast C-rate of 26 C. Moreover, the microelectrochemical method was employed as a platform to study the limiting step in the ion-electron transfer by modulating the C-rate. Mn-based PBA for negative and positive electrode processes were investigated using multi-sweep cyclic voltammetry concerning Na^+-based electrolytes with varying ionic strengths and counter anions. High stability of MnHCF (positive electrode) in highly concentrated $NaClO_4$ was established using multi-sweep CVs. However, galvanostatic evaluation of MnHCF at 20 C showed a drop of 30% in CE after just 30 cycles and an unstable response of the capacity. These results were further supported by optical imaging of the rME, ex-situ ICP-MS of the electrolyte, and *operando* Raman microspectroscopy measurements indicating dissolution of MnHCF during cycling as the main factor for the loss in capacity. The evaluation of Na^+-based electrolytes was extended to MnHCMn PBA (for the negative electrode). Low values of coulombic efficiency were obtained in 1 M Na^+-based electrolytes, with high capacity stability in 1 M NaSCN at 20 C. Despite a significant increase in %CE obtained in highly concentrated electrolytes (10 M NaSCN), a loss in the capacity of MnHCMn was observed during cycling. The effect of side reactions, e.g. with O_2, the electrolyte concentration which defines the ionic strength and hence the availability of free water/Na^+/anion was investigated concerning the MnHCMn performance. The proposed rME platform was demonstrated as an effective tool for accelerated material investigation utilizing a small amount of material while offering a qualitative assessment of the solid material performance in various electrolytes.

Experimental Section

Chemicals

All electrolytes were prepared with highly pure chemicals and ultra milliQ water (18 MΩ.cm). HCl and H_2SO_4 were purchased from Sigma–Aldrich. Au microelectrodes were prepared from borosilicate glass capillaries (Hilgenberg) and gold wire (100 μm diameter, Goodfellow). Manganese (III) acetate dihydrate [$Mn(CH_3COO)_3 \cdot 2H_2O$, 97%] was purchased from Merck, Manganese (II) nitrate tetrahydrate [$Mn(NO_3)_2$ 4 H_2O, (≥97%), potassium hexacyanoferrate (III) [$K_3Fe(CN)_6$, ≥99.0%] and potassium cyanide [KCN, ≥97.0%] were purchased from Sigma–Aldrich. Ethanol [absolute, 99.8%] was from ThermoFisher. A Schlenk line with Ar as an inert gas was used for nanoparticle synthesis and an Ar-filled glovebox was used for storing and handling air-sensitive as well as moisture-sensitive chemicals and materials.

Preparation of Recessed Gold-Disk Microelectrodes and PBA Filling Procedure

Microelectrodes (ME) were fabricated by sealing a Au wire with a diameter of 100 μm radius inside a borosilicate glass capillary. The Au-disk ME was characterized by CV in 0.5 mol/L H_2SO_4 solution. Recessed microelectrodes were obtained by electrochemical etching of the Au in 6 M HCl by means of CVs at a scan rate of 200 mV/s (20 cycles).[24] The resulting recessed depth of the rME was investigated using an optical microscope, SEM, as well as electrochemical characterization (16.5 μm), Figure S1.1. The rME was filled by mechanically pressing the rME against the PBA material powder placed in a weighing boat. PBA particles were kept inside an argon-filled glovebox (O_2 level below 0.2 ppm and H_2O level <0.1 ppm) before rME filling. The filling of PBA@rME was confirmed using an optical microscope (Figure S1.2). For more details see the SI.

Electrochemical Evaluation of PBA@rME

Electrochemical measurements were performed in a custom 3D-printed polymer-based electrochemical cell in a three-electrode configuration. A Pt coil served as a counter electrode and a Ag/AgCl/3 M KCl was used as a reference electrode. The working electrode was the recessed Au microelectrode (100 μm diameter). Before filling the PBA into the rME, the empty cavity was cleaned by ultrasonication. CVs in a potential range from 0 to 1.2 V vs Ag/AgCl/3 M KCl with a scan rate of 100 mV/s in 50 mM H_2SO_4 were performed for further electrochemical cleaning. After filling the rME with the PBA material, multi-sweep CVs were recorded using the PBA@rME as WE in different aqueous electrolytes. Electrolytes were purged with argon before filling the electrochemical cell. Afterwards, stability was evaluated by galvanostatic (dis)charge cycles with an applied constant current calculated to reach the predefined C-rate.

The set-up was adapted to maintain an inert atmosphere. The electrochemical cell, which is shown in Scheme 1b and Figure S1.2c, was placed inside a glass chamber (see Figure S4.2) consisting of a bottom and a top container. Both glass containers had an opening as an outlet for continuously purging the system with a flux of Ar. These openings were also used for the cables connecting the electrodes. The argon flux was bubbled through water to ensure water saturation before it was bubbled through the electrolyte for 1 h before the start of the electrochemical measurements.

Synthesis and Characterization of NiHCF

NiHCF particles were obtained following a procedure described before.[51] The resulting NiHCF particles were characterized by SEM imaging using a Quanta 3D FEG (FEI) operated at 30.0 kV in the high-vacuum mode. The SEM image in Figure S2.1a shows the shapes and non-uniform sizes of NiHCF particles. The X-ray diffractogram (Figure S2.1b) is consistent with the previously reported XRD patterns for NiHCF.[36]

Synthesis and Characterization of Mn[Fe(CN)$_6$] (MnHCF) and K$_2$Mn[Mn(CN)$_6$] (MnHCMn) Nanoparticles

Mn[Fe(CN)$_6$] was prepared by modifying a previously published synthesis procedure.[52] In short, 2.895 g of $Mn(CH_3COO)_3$ 2 H_2O (10.8 mmol) were dissolved in 18 mL water in a 50 mL centrifuge tube (solution A), and 1.185 g $K_3Fe(CN)_6$ (3.6 mmol) were dissolved in 18 mL water in a second 50 mL centrifuge tube (solution B). Solution A was dropwise poured into solution B (3 mL/min) under constant stirring (1100 rpm) at room temperature. The color of the solution changes quickly from light yellow to dark brown. Stirring is maintained for 30 min after the end of the addition. After centrifugation (3 min, 7000 rpm) the supernatant was discarded, and the separated particles were washed with water (2×10 mL) and ethanol (2×10 mL) and centrifuged after each washing step (3 min, 7000 rpm). The particles were dried overnight under a vacuum.

$K_2Mn[Mn(CN)_6]$ particles were prepared by modifying a known synthesis procedure,[4] 1.880 g of $Mn(NO_3)_2$ 4 H_2O (7.5 mmol) were dissolved in 30 mL water in a 100 mL 3-necked round bottom flask (solution A), and 2.440 g of KCN (37.5 mmol) were dissolved in 30 mL water in a 100 mL 3-necked round bottom flask (solution B). Solution B was dropwise poured into solution A dropwise (3.5 mL/min) under constant stirring (1100 rpm) at room temperature. The color of the solution changed quickly from light yellow to blueish green. Stirring was maintained for 30 min. The particles were aged for 20 h in the fume hood without stirring. The solution was transferred to a centrifuge tube and centrifuged (3 min, 7000 rpm) to separate the particles. The obtained particles were washed with water (2×15 mL) and ethanol (2×15 mL) and centrifuged after each washing step (3 min, 7000 rpm). The particles were dried overnight under vacuum and kept in an Ar-filled glovebox (O_2 level <0.1 ppm, H_2O level <0.1 ppm) prior to the electrochemical tests. For all samples, the morphology was evaluated using scanning electron microscopy (SEM) with a Carl Zeiss Merlin Compact VP. The crystalline structure was recorded using a Bruker D8 ADVANCE X-ray diffractometer with Cu Kα radiation (λ = 1.5406 Å) from 10 to 60°. The elemental ratio between Mn and Fe is derived from the stoichiometry of the reactants in the synthesis. Figure S3.1 and S4.1 summarized the results for MnHCF and MnHCMn, respectively.

Ex-Situ ICP-MS Measurements

Dissolution of MnHCF was studied using an inductively coupled plasma mass spectrometer (ICP-MS) Thermofischer iCAP RQ ASX-560. The electrolytes were diluted to around 100 mM $NaClO_4$ and acidified with 2% HNO_3. Prior to the detection of the dissolved metal, the instrument was calibrated for Mn and Fe using a seven-point calibration slope obtained from a standard solution. Nitric acid was aspirated between the samples to monitor the performance of the ICP-MS system. The cumulative amount of dissolved MnHCF during the galvanostatic cycles was measured with respect to the electrolyte.

Operando Raman Microspectroscopy

Raman measurements were performed on a Lab-RAM HR Raman microscopy system (Horiba Jobin Yvon HR550) with a 532 nm laser, a water immersion objective (Olympus LUMFL, 60x, numerical aperture 1.10), a monochromator (grating 1200 grooves/mm), and a Synapse CCD detector. The custom-made 3D-printed open cell was adapted to fit the upside-down positioned rME with a shallow depth to enable the water immersion objective to be very close to the rME. The rME was positioned using the motor for fine movements and aligned with the laser beam (Figure S3.5). A Ag/AgCl/3 M KCl electrode was used as reference electrode, and a Pt wire was used as counter electrode, in 5 M $NaClO_4$. *Operando* electrochemical Raman measurements were performed using an AUTOLAB potentiostat in a potential range from 0 to −0.8 V vs Ag/AgCl/3 M KCl.

Supporting Information

More details about the electrochemical measurements and material characterization are found in the Supporting Information. The authors have cited additional references in the Supporting Information.[53]

Acknowledgements

The authors acknowledge funding from the European Union's Horizon Europe research and innovation programme – European Innovation Council (EIC) under the grant agreement 101046742 (MeBattery), the European Research Council (ERC) under the European Union's Horizon 2020 research and innovation programme (CasCat [833408]), and the Spanish Government (Ministerio de Ciencia e Innovación, Grants

PID2021-124974OB-C22). The authors thank Martin Trautmann (RUB) and Prof. Dr. Daniel Grasseschi (Federal University of Rio de Janeiro – UFRJ) for support concerning ICP-MS and Raman measurements, respectively. Open Access funding enabled and organized by Projekt DEAL.

Conflict of Interests

The authors declare no conflict of interest.

Data Availability Statement

The data that support the findings of this study are available from the corresponding author upon reasonable request.

Keywords: Prussian blue analogues · recessed microelectrode · microelectrochemistry · sodium-ion battery · Mn-hexacyanomanganate

[1] J. Liu, C. Yang, B. Wen, B. Li, Y. Liu, *Small* **2023**, *19*, e2303896.
[2] C. D. Wessells, Chapter 7 in *Na-ion Batteries*, Wiley, **2021**, Volume 1, pp. 265–311.
[3] Z. Li, B. Ozdogru, B. Bal, M. Bowden, A. Choi, Y. Zhang, H. Wang, V. Murugesan, V. G. Pol, Ö. Ö. Çapraz, *Adv. Energy Mater.* **2023**, *13*, 2301329.
[4] V. Renman, D. O. Ojwang, C. Pay Gómez, T. Gustafsson, K. Edström, G. Svensson, M. Valvo, *J. Phys. Chem. C* **2019**, *123*, 22040–22049.
[5] C. D. Wessells, S. V. Peddada, R. A. Huggins, Y. Cui, *Nano Lett.* **2011**, *11*, 5421–5425.
[6] V. Renman, D. O. Ojwang, C. Pay Gómez, T. Gustafsson, K. Edström, G. Svensson, M. Valvo, *J. Phys. Chem. C* **2019**, *123*, 22040–22049.
[7] Y. Zeng, Y. Wang, Z. Huang, H. Luo, H. Tang, S. Dong, P. Luo, *Nanotechnology* **2023**, *34*, 475403.
[8] N. Kitchamsetti, *J. Energy Storage* **2023**, *73*, 108958.
[9] J.-G. Wang, Z. Zhang, X. Zhang, X. Yin, X. Li, X. Liu, F. Kang, B. Wei, *Nano Energy* **2017**, *39*, 647–653.
[10] C. Zhang, T. Wang, Y. Han, Z. Wang, B. Luo, K.-J. Chen, *J. Power Sources* **2024**, *607*, 234576.
[11] C. D. Wessells, M. T. McDowell, S. V. Peddada, M. Pasta, R. A. Huggins, Y. Cui, *ACS Nano* **2012**, *6*, 1688–1694.
[12] S. Wheeler, I. Capone, S. Day, C. Tang, M. Pasta, *Chem. Mater.* **2019**, *31*, 2619–2626.
[13] J. Peng, W. Zhang, Q. Liu, J. Wang, S. Chou, H. Liu, S. Dou, *Adv. Mater.* **2022**, *34*, e2108384.
[14] Y. Matos-Peralta, M. Antuch, *J. Electrochem. Soc.* **2020**, *167*, 37510.
[15] a) S. Porada, A. Shrivastava, P. Bukowska, P. M. Biesheuvel, K. C. Smith, *Electrochim. Acta* **2017**, *255*, 369–378; b) J. Lee, S. Kim, J. Yoon, *ACS Omega* **2017**, *2*, 1653–1659.
[16] F. Zhang, S. Huang, X. Wang, C. Jia, Y. Du, Q. Wang, *Nano Energy* **2018**, *52*, 292–299.
[17] X. Lamprecht, F. Speck, P. Marzak, S. Cherevko, A. S. Bandarenka, *ACS Appl. Mater. Interfaces* **2022**, *14*, 3515–3525.
[18] W.-J. Li, C. Han, G. Cheng, S.-L. Chou, H.-K. Liu, S.-X. Dou, *Small* **2019**, *15*, e1900470.
[19] A. Vertova, R. Barhdadi, C. Cachet-Vivier, C. Locatelli, A. Minguzzi, J.-Y. Nedelec, S. Rondinini, *J. Appl. Electrochem.* **2008**, *38*, 965–971.
[20] S. Barwe, C. Andronescu, J. Masa, E. Ventosa, S. Klink, A. Genç, J. Arbiol, W. Schuhmann, *ChemSusChem* **2017**, *10*, 2653–2659.
[21] M. Nebel, T. Erichsen, W. Schuhmann, *J. Nanobiotechnol.* **2014**, *5*, 141–151.
[22] J. Behnken, M. Yu, X. Deng, H. Tüysüz, C. Harms, A. Dyck, G. Wittstock, *ChemElectroChem* **2019**, *6*, 3460–3467.
[23] J. Clausmeyer, P. Actis, A. López Córdoba, Y. Korchev, W. Schuhmann, *Electrochem. Commun.* **2014**, *40*, 28–30.
[24] R. A. Rincón, A. Battistel, E. Ventosa, X. Chen, M. Nebel, W. Schuhmann, *ChemSusChem* **2015**, *8*, 560–566.
[25] C. Locatelli, A. Minguzzi, A. Vertova, P. Cava, S. Rondinini, *Anal. Chem.* **2011**, *83*, 2819–2823.
[26] C. Cachet-Vivier, V. Vivier, C. S. Cha, J.-Y. Nedelec, L. T. Yu, *Electrochim. Acta* **2001**, *47*, 181–189.
[27] B. Zhang, Y. Zhang, H. S. White, *Anal. Chem.* **2004**, *76*, 6229–6238.
[28] B. Zhang, J. Galusha, P. G. Shiozawa, G. Wang, A. J. Bergren, R. M. Jones, R. J. White, E. N. Ervin, C. C. Cauley, H. S. White, *Anal. Chem.* **2007**, *79*, 4778–4787.
[29] T. Löffler, J. Clausmeyer, P. Wilde, K. Tschulik, W. Schuhmann, E. Ventosa, *Nano Energy* **2019**, *57*, 827–834.
[30] C. Santana Santos, T. Quast, E. Ventosa, W. Schuhmann, *ChemElectroChem* **2024**, *11*, e202400283.
[31] X. Lamprecht, F. Speck, P. Marzak, S. Cherevko, A. S. Bandarenka, *ACS Appl. Mater. Interfaces* **2022**, *14*, 3515–3525.
[32] E. Ventosa, *Curr. Opin. Electrochem.* **2021**, *25*, 100635.
[33] C. Cachet-Vivier, M. Keddam, V. Vivier, L. T. Yu, *JEAC* **2013**, *688*, 12–19.
[34] W. Ren, M. Qin, Z. Zhu, M. Yan, Q. Li, L. Zhang, D. Liu, L. Mai, *Nano Lett.* **2017**, *17*, 4713–4718.
[35] W. Ren, M. Qin, Z. Zhu, M. Yan, Q. Li, L. Zhang, D. Liu, L. Mai, *Nano Lett.* **2017**, *17*, 4713–4718.
[36] M.-W. Zheng, H.-K. Lai, K.-Y. A. Lin, *Waste Biomass Valor* **2019**, *10*, 2933–2942.
[37] T. Huang, G. Du, Y. Qi, J. Li, W. Zhong, Q. Yang, X. Zhang, M. Xu, *Inorg. Chem. Front.* **2020**, *7*, 3938–3944.
[38] Y. Shang, X. Li, J. Song, S. Huang, Z. Yang, Z. J. Xu, H. Y. Yang, *Chem* **2020**, *6*, 1804–1818.
[39] A. Choi, T. Kim, M.-H. Kim, S. W. Lee, Y. H. Jung, H.-W. Lee, *Adv. Funct. Mater.* **2022**, *32*, 2111901.
[40] J. Peng, Y. Gao, H. Zhang, Z. Liu, W. Zhang, L. Li, Y. Qiao, W. Yang, J. Wang, S. Dou, S. Chou, *Angew. Chem. Int. Ed.* **2022**, *61*, e202205867.
[41] J. Liu, C. Yang, B. Wen, B. Li, Y. Liu, *Small* **2023**, *19*, e2303896.
[42] J. Cattermull, M. Pasta, A. L. Goodwin, *J. Am. Chem. Soc.* **2023**, *145*, 24471–24475.
[43] M. Fayaz, W. Lai, J. Li, W. Chen, X. Luo, Z. Wang, Y. Chen, D. Li, S. M. Abbas, Y. Chen, *Mater. Res. Bull.* **2024**, *170*, 112593.
[44] H.-W. Lee, R. Y. Wang, M. Pasta, S. Woo Lee, N. Liu, Y. Cui, *Nat.Comm.* **2014**, *5*, 5280.
[45] M. Pasta, C. D. Wessells, N. Liu, J. Nelson, M. T. McDowell, R. A. Huggins, M. F. Toney, Y. Cui, *Nat. Commun.* **2014**, *5*, 3007.
[46] J. Yun, J. Pfisterer, A. S. Bandarenka, *Energy Environ. Sci.* **2016**, *9*, 955–961.
[47] M. L. Miller, M. Doran, *J. Phys. Chem.* **1956**, *60*, 186–189.
[48] A. Asserghine, S. Kim, T. P. Vaid, A. Santiago-Carboney, A. J. McNeil, J. Rodríguez-López, *ACS Energy Lett.* **2024**, *9*, 2826–2831.
[49] C. Geng, D. Buchholz, G.-T. Kim, D. V. Carvalho, H. Zhang, L. G. Chagas, S. Passerini, *Small Methods* **2019**, *3*, 1800208.
[50] L. S. Kremer, T. Danner, S. Hein, A. Hoffmann, B. Prifling, V. Schmidt, A. Latz, M. Wohlfahrt-Mehrens, *Batteries & Supercaps* **2020**, *3*, 1172–1182.
[51] R. Trócoli, A. Battistel, F. La Mantia, *ChemSusChem* **2015**, *8*, 2514–2519.
[52] M. Xu, Q. Zhang, Z. Zhu, Y. Xue, T. Zhang, J. Hong, *J. Cleaner Prod.* **2022**, *377*, 134258.
[53] E. Torralba, E. Laborda, A. Molina, C. Cachet-Vivier, S. Bastide, *ChemElectroChem* **2021**, *8*, 735–744.

Manuscript received: November 24, 2024
Revised manuscript received: December 20, 2024
Accepted manuscript online: December 24, 2024
Version of record online: January 23, 2025